An Experimental and Theoretical Study of the Turbulent and Laminar Convection Generated under a Horizontal Ice Sheet Floating on Warm Salty Water

SEELYE MARTIN

Department of Oceanography, University of Washington, Seattle 98195

PETER KAUFFMAN

Department of Atmospheric Sciences, University of Washington, Seattle 98915

(Manuscript received 14 May 1976, in revised form 7 October 1976)

ABSTRACT

In an experimental and theoretical study we model a phenomenon which occurs in the summer polar oceans; namely, the melting of flat sheets of either glacial ice or desalinated sea ice which float over sea water held at a temperature above freezing. Our laboratory results show when the solution salinity is such that the temperature of maximum density is below the freezing temperature, or for sea water salinities greater than 25‰, the heat transfer to the ice takes place in three regions. First, just beneath the ice, there is a boundary layer across which the salinity increases almost to its far-field value and the temperature increases linearly. Below this, there is an unstable convective boundary layer, which appears to be part double-diffusive, part pure thermal convection. Finally, there is a region of deep thermal convection. From comparison of a one-dimensional theoretical model of the heat transfer with the laboratory study, we find that the ice melts about twice as fast for this convective case as for a purely diffusive heat transfer model.

1. Introduction

The bottom side of a horizontal block of fresh-water ice floating in warm, salty water melts through the combination of thermal and salinity boundary layers. Physically, such melting occurs under both glacial ice and desalinated sea ice, and is driven in the following ways. For glacial ice, this melting occurs at the bottom of icebergs when they are advected into temperate waters. For sea ice, during the summer the solar radiation absorbed in leads, polynyas and through the ice heats the sea water above the freezing point. For that part of the sea ice which is both nearly salt-free and extends below the depth of the summer low-salinity surface layer caused by runoff from the ice [see Coachman and Barnes (1962) for discussion], the solar heating may drive a similar melting.

In both cases, the melting cools and dilutes the adjacent water at the ice block. The present paper shows that if the sea-water salinity is greater than 25‰ then the heat transfer to the ice occurs in three regions. First, directly beneath the ice, there is a region of conductive heat transfer across which the salinity increases almost to its far-field value; second, beneath this conductive region there is an unstable convective boundary layer; third, below the boundary layer there is a region of deep thermal convection.

Two physical factors cause the turbulent convection. First, the thermal diffusivity is about 10^3 times the salt diffusivity, so that the thermal disturbance generated by the melting ice tends to propagate further than the salt disturbance. Second, because the thick thermal boundary layer is colder than the underlying water and since cooling sea water of salinity $>$ than 25‰ (23‰ for NaCl solutions) makes the water heavier, a convectively unstable region forms. This convection increases the heat transfer to the ice over that predicted from a purely diffusive calculation.

In the following, we describe a laboratory model of the melting, then derive a theoretical model of the process which we compare with the experiment.

2. The experiment

The experiment took place in a Plexiglas tank 0.45 m $\times$0.45 m in cross-section and 0.90 m deep, which was filled to a depth of 0.75 m with a 37.6‰ NaCl solution (Fig. 1). To prevent heat transfer through the side walls, we surrounded the sides and bottom of the tank with 75 mm of polyurethane foam. During the experiment, we placed the tank in a cold room at the temperature of 0°C$\pm$2°C. To keep the water at a constant temperature, we circulated ethanol from a constant temperature bath through a closed loop of stainless steel

tubing placed near the bottom of the tank. The circulating ethanol maintained the temperature in the lower part of the tank very close to 0°C.

On the surface of the salt water, we floated a block of bubble-free fresh-water ice. The ice was 0.1 m in thickness, and we cut the sides of the block so that the block fit precisely in the tank. Before placing the block in the tank, we cut a hole 50 mm in diameter vertically through the ice block along the diagonal connecting two opposing corners at a point 0.21 m in from one corner for the thermocouple array. The array consisted of 18 copper-constantan thermocouples mounted at the depths shown on the left-hand side of Figs. 2 a–e. The thermocouples were enclosed in glass tubing and positioned at a distance of 10 mm from a central Plexiglas support which encased the leads. This array was identical to that used by Martin and Kauffman (1974, hereafter abbreviated as MK). We read the position of the ice-water interface from a ruler attached to the temperature array; the large index of refraction change adjacent to the block limited our reading accuracy to ± 0.25 mm. To fix the array into the ice block, we set the array in the hole at the desired depth, and then packed ice chips around it. Then, with the room temperature set below 0°C, we slowly poured fresh water at 0°C into the hold until solid ice formed around the array.

The experiment began when we placed the array, ice block combination into the tank. The array was then connected through a scanner and a nanovolt amplifier to a magnetic tape recorder. Every 2 min, this system scanned the array and stored the data on magnetic tape. Our nanovolt amplifier coupled to a $5\frac{1}{2}$ digit display digital voltmeter allowed us to measure thermocouple voltages to ± 0.1 μV, or to $\pm 3 \times 10^{-3}$ °C. We measured the drift of this system by placing both a calibration and reference thermocouple separated by a distance of 50 mm in our reference ice bath. The ice bath consisted of a Dewar flask, which was completely surrounded by 50 mm of polyurethane foam, containing 4 liters of de-ionized water and the ice grown from this water. On each system scan, we recorded the offset of the calibration thermocouple relative to the reference thermocouple; examination of this record showed that the system drift was about ± 0.1 μV and that the absolute accuracy was on the order of $\pm 10^{-2}$ °C.

To measure the salinity, we withdrew water samples through holes in one side of the tank. The holes, which were 6.4 mm in diameter, were spaced at 20 mm intervals in the vertical, and plugged with Dow Corning RTV silicone rubber. We took samples by inserting a #24 hypodermic needle of length 70 mm in through the plug, then withdrawing 3 ml of brine into a syringe. By tilting the needle up or down from the horizontal, we sampled the salinities at positions between the plugs. The plug resealed when we withdrew the needle. We determined the salinities of these samples through coulometric titration, which yielded accuracies of 0.1‰. During the course of the experiment, we sampled salinity at approximately twice-daily intervals.

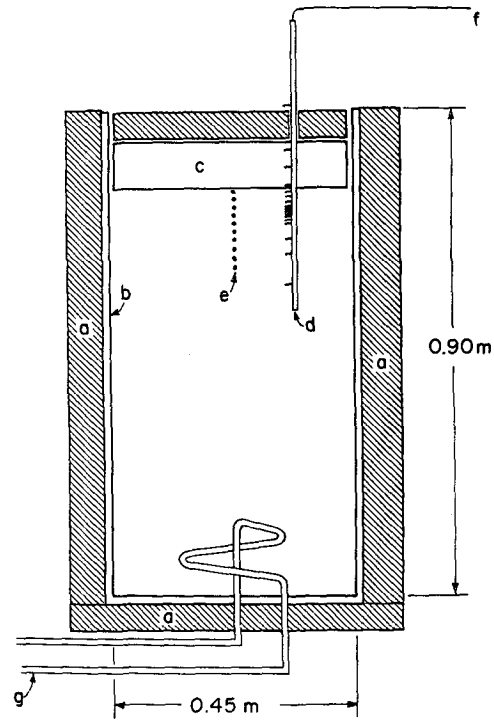

FIG. 1. A schematic diagram of the apparatus: (a) polyurethane insulation, (b) Plexiglas tank, (c) fresh-water ice block, (d) thermocouple array, (e) holes for salinity sampling, (f) cable to digitizer, and (g) tube for the circulating alcohol.

When we placed the ice block into the tank, the ice bottom was not perfectly flat, but had small bumps on its surface extending down 1–2 mm as well as a few cubic centimeters of crushed ice frozen around the 10 mm length of the array which was just beneath the interface. Relative to the ruler on the array, we estimated the initial interface position as -3 mm. By 3.5 h after the experiment began, the interface was flat at -2.0 mm. We also found that thermal transients accompanied the beginning of the experiment. From the thermocouples, we observed that the placement of the ice block into the tank generated a cold thermal transient which propagated up into the ice. Also, the melting of both the ice bumps and the crushed ice on the bottom of the ice block generated some additional local cooling near the ice wall. Finally, for the first 19 h of the experiment, heating from the alcohol circulator caused the deep temperature as measured by the probe at -23 cm to increase from -0.1°C to $+0.05$°C, at which point the temperature stabilized.

From visual observations of the ice block, we discovered that the salt water which flowed up into the small gap between the ice block sides and the Plexiglas walls at first froze into the gap, then began laterally to melt the ice walls. This melting qualitatively appeared to result from the following effects: a weak heat flux

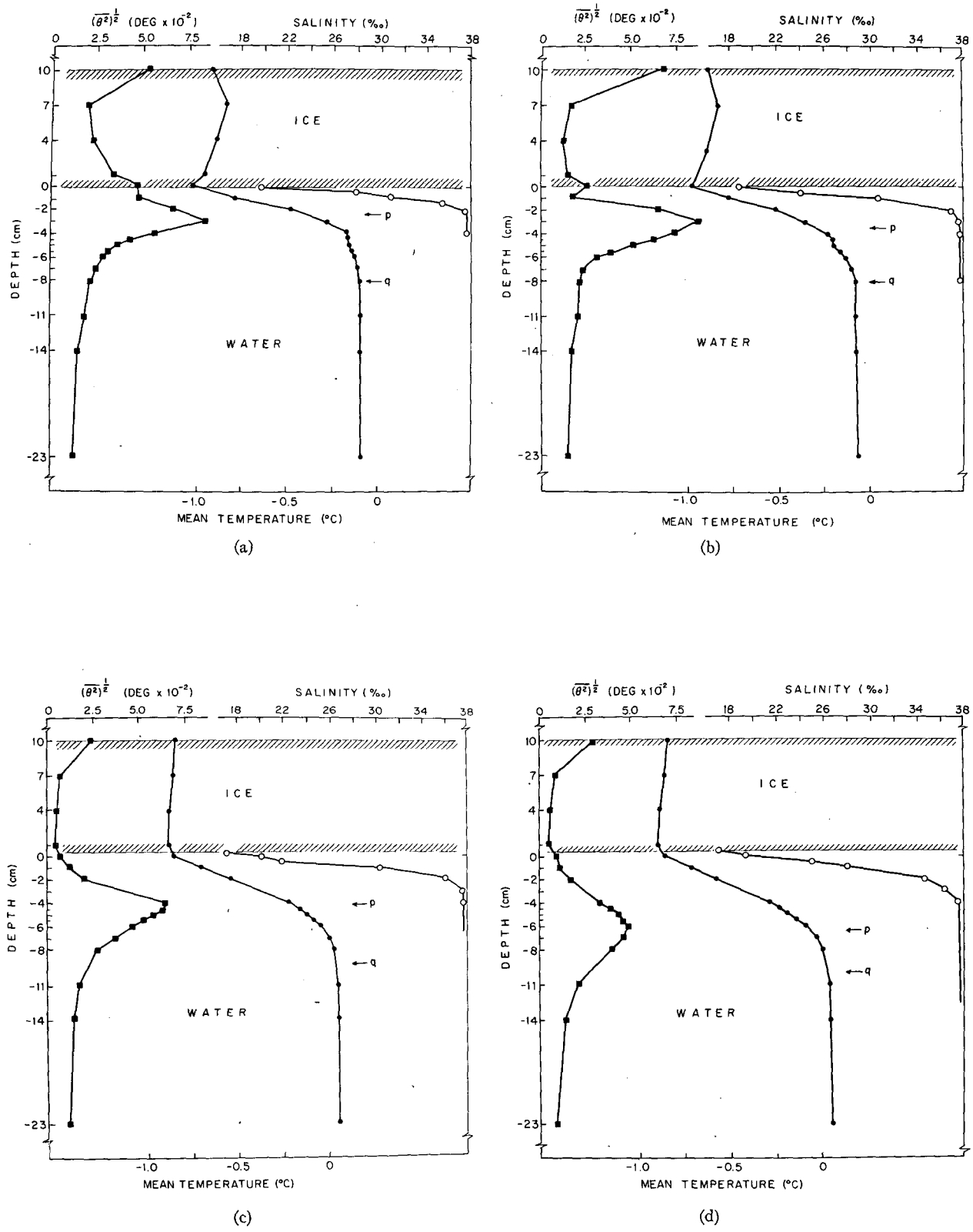

FIG. 2. Observed profiles of mean temperature and salinity and rms temperature fluctuations $(\overline{\theta^2})^{\frac{1}{2}}$: (■) rms fluctuations, (●) mean temperature, (○) mean salinity. The probe at −3 cm failed at 19 h; the levels p and q are explained in the text. (a) 5.5 h into the experiment; (b) 7.5 h; (c) 21.0 h; (d) 26.5 h; (e) 46.5 h.

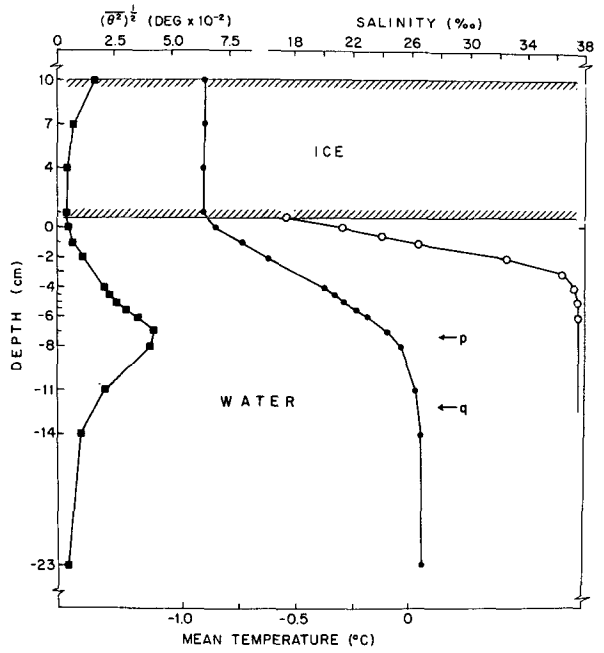

(e)

in through the tank walls; the transfer of heat by the upward flow into the gap of the warm, less saline water generated by the melting; and the heat transfer process studied by MK (see Section 4) which occurs when a fluid with salinity and temperature gradients is adjacent to a vertical ice wall. The effect on the ice was that after one day, although the top of the ice block was still frozen to the side walls, the lower corners had melted inward by about 10 mm. After two days, the inward melting continued and the ice block bottom developed a curvature which extended horizontally in about 100 mm from the side walls with a vertical height change of 1 mm. Because of this developing curvature, we only analyzed data from the first two days of the experiments.

When the experiment was over, we both printed and plotted out the temperatures. We then took several 4 h data segments and calculated both the mean temperatures and the rms temperature fluctuations at the different depths and at several times throughout the experiment corresponding to the times of our salinity samples. Figs. 2 a–e are plots of the depth variation of the rms fluctuations, the mean temperatures and the salinities. For Fig. 2a, we took the salinity sample at the beginning of the averaging period; while for the other four figures, the salinity sample falls in the middle of the averaging period. At the ice wall, the salinity is not sampled directly; rather we calculate this salinity from the observed temperature and the freezing point depression of NaCl, which is given by Eq. (1a). Also on Figs. 2 a–e, the letter p marks the depth of the rms temperature fluctuation maximum as extrapolated from the measured points; q marks the depth at which the mean temperature profile below p intercepts a straight line drawn through the deep temperatures. The depth p falls slightly below that depth at which the salinity profile attains its far-field value; we suspect from our later analysis that because our salinity measurements are only accurate to 0.1‰, some slight salinity variation exists at p.

Figs. 3 and 4 show plots of the raw temperature data at various depths within the fluid across the depth p for two different 12 h periods. On Fig. 3, all of the profiles show some warming with time, the cause of which is a combination of the disappearance of the transients generated by the melting of the ice bumps on the interface and the heating from the alcohol circulator. The figure, which includes the temperature data averaged for Figs. 2a and 2b, shows how the nature of the temperature profiles change as to whether they are above, at or below the depth p. First, the profile labeled 1 which is both above p and well within the salinity boundary layer, shows damped thermal oscillations. Second, the fluctuations on profiles 2 and 3, which are at depths close to p on Figs. 2a and 2b, consist of sharp spikes separated by quiescent periods; these profiles are characteristic of those caused by thermal convective plumes (Turner, 1973, Section 7.3.1). Profile 2 shows that the magnitudes of these fluctuations decreases as the salinity layer advances over the probe. Below p,

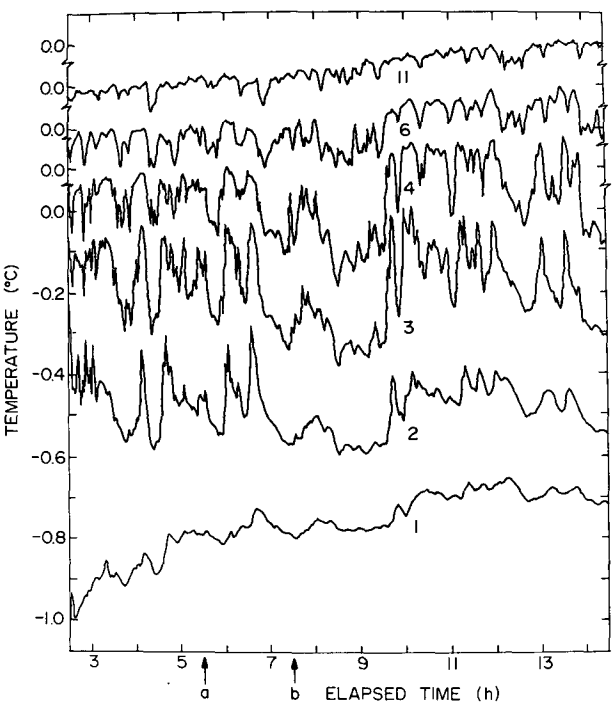

FIG. 3. Plots of temperature at several depths and versus time from 2.5 to 14.5 h into the experiment. The numbers under the curves are the thermistor depths (cm) below the depth origin on Figs. 2; the top four profiles are each offset by 0.1°C from the profile below. Beneath the time scale, the letters a and b show the sample time of Fig. 2a and 2b.

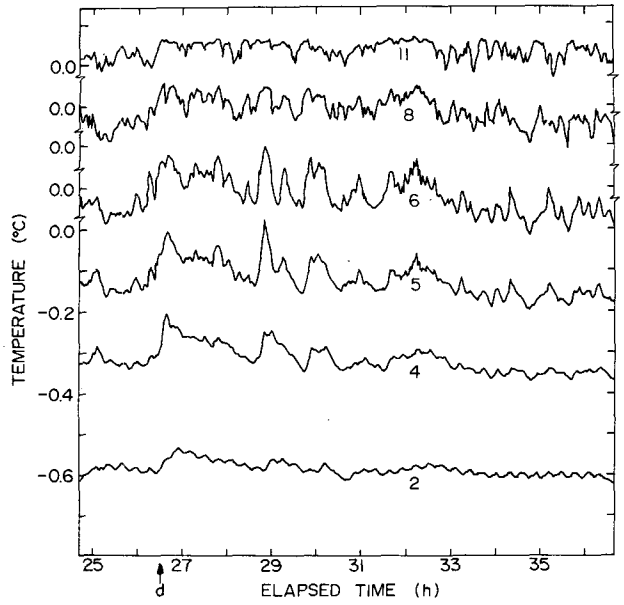

FIG. 4. Plots of temperature at several depths and versus time for the time period from 24.67 to 36.67 h. See also legend of Fig. 3. The letter d beneath the time scale shows the sample time of Fig. 2d.

profiles 4, 6 and 11 show that the fluctuation magnitudes also decrease as the depth below the salinity layer increases.

Fig. 4, which begins 11 h after the end of the time series in Fig. 3 and includes the data averaged for Fig. 2d, shows that the fluctuation amplitudes have decreased well below those shown in Fig. 3. For this figure, profiles 2 and 4 are above p and within the salinity layer; 5 and 6 are very close to p; and 8 and 11 are below p. The small fluctuations which occur on profile 2 with an amplitude of 10^{-2} °C and a period of about 20 min are an example of the noise induced by the cold room fluctuations. The cause of this noise, which is much smaller than the convective fluctuations and does not appear on the calibration thermocouple record, is apparently due to the propagation into the tank in a greatly attenuated form of the cold room fluctuations. From the other profiles, we again see that the large temperature fluctuations appear to propagate downward as plumes, and up into the salinity boundary layer as damped, slightly phase-shifted signals.

Returning to Fig. 2, we find that the mean profiles show the following interesting results. First, above the depth p the mean temperature increases nearly linearly with depth from the ice wall to p. Below this depth the mean profile curves off to the asymptote of the interior temperature profile at q. Second, if we take the distance between the ice wall and either the depth p or q as characteristic of a temperature boundary layer thickness, then we see from the figures that the thicknesses of the temperature and salinity boundary layers are of the same order. Third, as the experiment goes on, the temperature in the ice interior becomes uniform; this simplifies our theoretical analysis. Fourth, the magnitude of the rms fluctuations is of the order of 10^{-1} °C, whereas the magnitude of the mean temperature difference between the wall and the rms maximum, which we call ΔT_w, is of the order of 1°C, so that the temperature fluctuations at p are small compared with ΔT_w.

Because the density increases as the temperature decreases below the salinity boundary layer, the data suggest that the heat transfer under the ice sheet divides into two parts. First, above the depth p the salinity stratification inhibits convection so that the heat transfer is conductive; below this depth the heat transfer is by convection. In the following analysis we first calculate the heat transfer for the case of purely diffusive heat and salt transfer. We then use these solutions both to show the time of onset of thermal instability for the experiment is of the order of 10^2 s, and for later comparison with a combined conductive-turbulent heat transfer model.

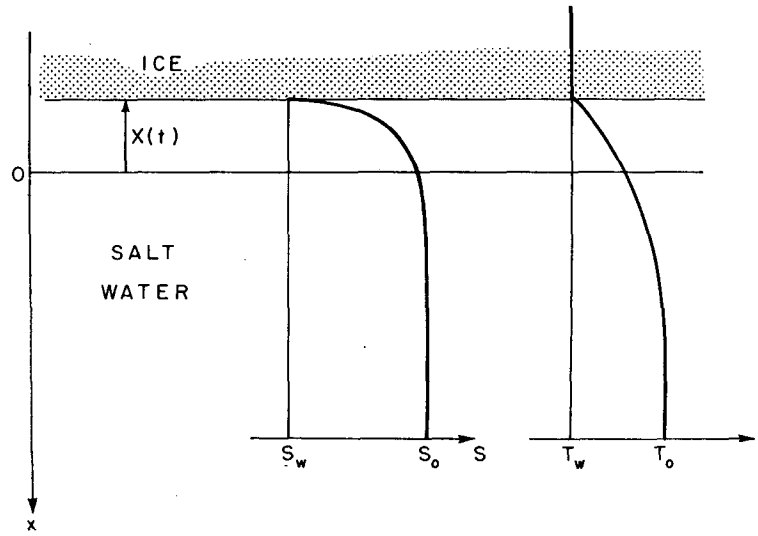

FIG. 5. A schematic diagram of the ice, salt water system.

3. The diffusive regime

a. The diffusive solution

Carslaw and Jaeger (1959, hereafter abbreviated CJ) solve the one-dimensional diffusion problem of ice melting in warm fresh water. For ice in warm salty water, we next show that the solution which describes the melting is a superposition of two of the CJ solutions with some complications introduced by the boundary conditions at the ice wall.

In our derivation, we assume that the temperature inside the ice is at a uniform to-be-solved-for wall temperature. Also, we assume in the fluid that one-dimensional diffusion equations with constant coefficients govern the flow of heat and salt. Fig. 5 shows our coordinate system, where x is length and t time. The height of the ice interface above the origin is given by $x=X(t)$, and the temperatue and salinity fields are respectively $T(x,t)$ and $s(x,t)$. The initial condition on the ice-water interface is at $t=0$, $X(t)=0$.

At the ice wall, following Frank (1950), we have three boundary conditions on s and T. First, the temperature and salinity must lie on the freezing or eutectic curve. From Kaufman (1960, p. 613) the dependence of the freezing point depression on salinity is nearly linear, so we write the freezing condition at the wall as

$$T+ms=0 \quad \text{at} \quad x=X(t) \tag{1a}$$

where $m=5.71\times10^{-2}$ °C. Second, the heat flux to the water caused by the wall melting is

$$\frac{\partial T}{\partial x}=\frac{L\rho_i}{k}\frac{\partial X}{\partial t} \quad \text{at} \quad x=X(t) \tag{1b}$$

where L is the latent heat of freezing, ρ_i the density of ice, and k the thermal conductivity. Third, the salt flux to the water is

$$\frac{\partial s}{\partial x}=-\frac{s}{D}\frac{\partial X}{\partial t} \quad \text{at} \quad x=X(t) \tag{1c}$$

where D is the salt diffusivity.

Away from the wall, our far field conditions are that

$$s=s_0, \quad T=T_0, \quad \text{as} \quad x\to\infty. \tag{2}$$

To simplify the subsequent calculations, we define H as the temperature elevation of the fluid in the far field above the freezing point, where

$$H=T_0+ms_0.$$

The solutions of the diffusion equations which satisfy the far field conditions are

$$T=T_0-A\ \text{erfc}u_T, \tag{3a}$$

$$s=s_0-B\ \text{erfc}u_s, \tag{3b}$$

where

$$u_T=\frac{x}{2(\kappa t)^{\frac{1}{2}}}, \quad u_s=\frac{x}{2(Dt)^{\frac{1}{2}}}, \tag{3c}$$

and κ is the thermal diffusivity. Following CJ and Frank (1950), we write the wall displacement as

$$X(t)=-2\lambda(\kappa t)^{\frac{1}{2}}=-2\gamma(Dt)^{\frac{1}{2}}, \tag{4}$$

where λ and γ are to-be-determined dimensionless constants. Since the wall moves with one velocity,

$$\frac{\lambda}{\gamma}=\left(\frac{D}{\kappa}\right)^{\frac{1}{2}}=\epsilon.$$

For our problem, $D=6\times10^{-10}$ m^2 s^{-1} [extrapolated from Caldwell (1974)] and $\kappa=1.4\times10^{-7}$ m^2 s^{-1} (CJ, Appendix 6), so that

$$\epsilon=6.6\times10^{-2}.$$

To solve the above problem, we must find A, B and λ as functions of s_0 and T_0. We do this in three steps.

First, substitution of (3) into the eutectic condition (1) gives

$$A=\frac{H-mB\ \text{erfc}(-\gamma)}{\text{erfc}(-\epsilon\gamma)}. \tag{5}$$

Second, substitution of (3a) and (4) into the heat flux condition (1b) gives

$$\lambda e^{\lambda^2}=A\frac{\alpha}{H}, \tag{6a}$$

where using the identity $k\equiv\rho c_p\kappa$ yields

$$\alpha=\frac{Hk}{2L\rho_i\kappa\pi^{\frac{1}{2}}}. \tag{6b}$$

The parameter α is proportional to the volume of ice melting divided by that volume of water, which when cooled through a temperature change H, would supply the heat to melt the ice. In our experiment, $\rho=1027$ kg m^{-3} [Kaufman (1960), Table 44, for $s=38‰$ and $T=0$°C], and $c_p=4.18$ kJ kg^{-1} °C^{-1}, $\rho_i=917$ kg m^{-3} and $L=334$ kJ kg^{-1} (all from CJ, Appendix 6). Since $H\approx1$°C, $\alpha\approx10^{-2}$.

To obtain the constant B in terms of s_0 and γ, we do a straightforward substitution of (3b) into (1c). Then, substitution of this result and A from Eq. (6) into (5) gives

$$\lambda e^{\lambda^2}\ \text{erfc}(-\lambda)=\alpha[1-rf(\gamma)], \tag{7a}$$

where

$$f(\gamma)=\frac{\gamma(\pi)^{\frac{1}{2}}\ \text{erfc}(-\gamma)}{e^{-\gamma^2}+(\pi)^{\frac{1}{2}}\ \text{erfc}(-\gamma)}, \tag{7b}$$

$$r=\frac{ms_0}{H}. \tag{7c}$$

The parameter r is the ratio of the salinity-caused freezing point depression to the temperature elevation H above freezing, and the function $f(\gamma)$ in product with r contains the effect of salinity on the mathematical

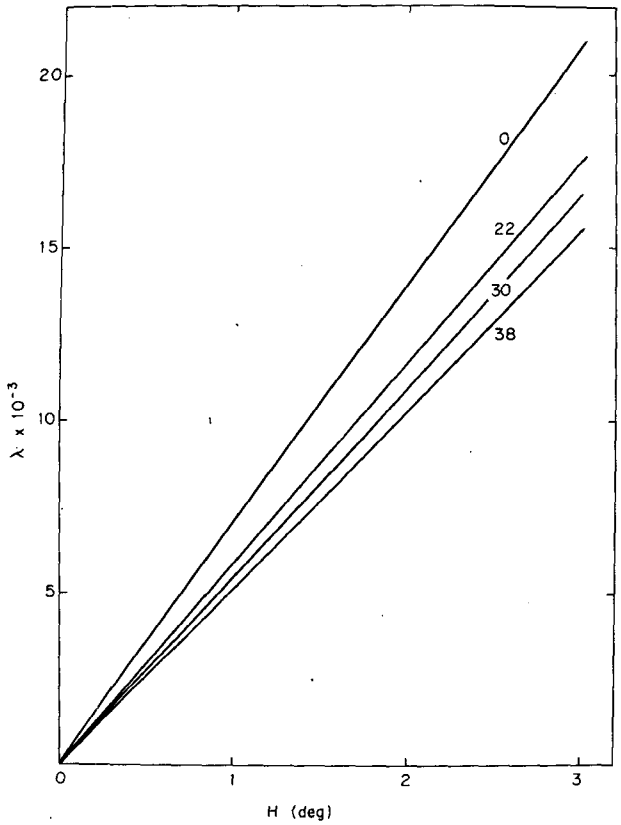

FIG. 6. The diffusive heat transfer case showing curves of λ plotted against H for the values of s_0 shown adjacent to each curve.

solution. When $r=0$, (7a) reduces to the fresh water case solved by CJ.

Eqs. (7) give λ as functions of α, r and ϵ. For different values of H and s_0, we numerically solved (7) with a simple iterative technique for λ. Fig. 6 shows some of the solution curves for λ plotted against H for different salinities. The upper curve shows the fresh water case, where H is the actual difference between the wall and far-field temperature. The lower curves give the melting rates for several salt water cases. The figure shows that as s_0 increases, the growth rate decreases. The physical reason for this decrease is that the melting of the ice wall dilutes the adjacent salt water. Because of the eutectic condition (1a), this dilution reduces the actual temperature difference between the wall and the far field below H, thus reducing the growth rate below that calculated for the fresh water case. As the solution salinity increases, the melting causes a relatively larger dilution, so that the growth rate decreases. For $s=38‰$, the growth rate is about two-thirds that of the fresh water case.

For the same salinities, Fig. 7 shows the variation in wall temperature T_w as a function of H. The figure indicates that as H increases from zero, the wall temperature increases above the far-field freezing point, so that the wall salinity decreases.

From λ, the constants A and B, and the solutions (3), we arrive at two independently diffusing solutions for salt and heat, with their respective boundary layer thicknesses in the ratio ϵ. Physically, the melting yields a very thin salinity layer inside of a broad temperature boundary layer. If the salinity of the sodium chloride solutions is greater than 23‰, then the temperature of maximum density lies below the freezing point, so that cooling solutions of this salinity increases the density. Therefore, the region of cold water of the ambient salinity which lies below the salinity boundary layer is the heaviest water in the tank. If this layer of heavy water becomes thick enough, convection occurs.

b. The convective instability

To estimate the time in which the diffusive solution becomes unstable, we assume that a thermal instability alone governs the onset of convection. For thermally unstable fluids, Howard [(1966), cited in Turner (1973)] shows when a horizontal flat plate is abruptly cooled from above, that the onset of convection in the boundary layer under the plate depends on the magnitude of the Rayleigh number

$$\mathrm{Ra}_\delta = \frac{\beta \Delta T g \delta^3}{\kappa \nu}, \tag{8a}$$

where β is the coefficient of thermal expansion, g the acceleration of gravity, δ the thickness of the unstable

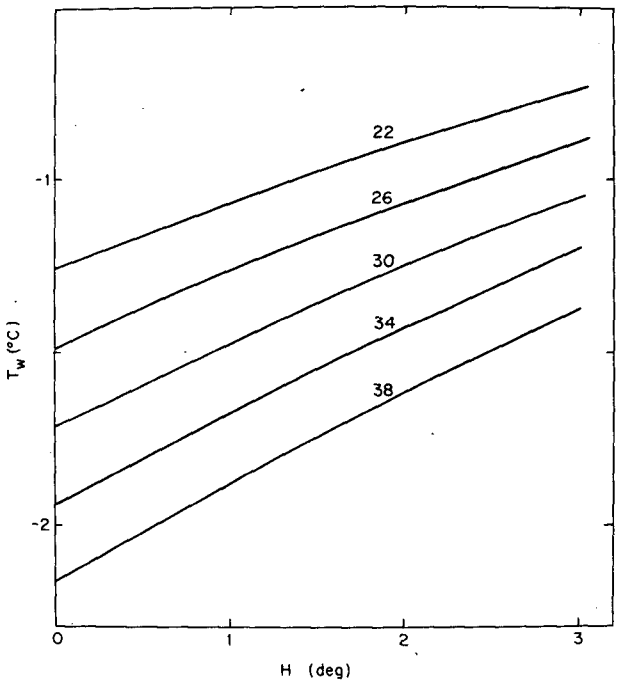

FIG. 7. The diffusive heat transfer case showing T_w plotted against H for the values of s_0 shown above each curve. The zero intercept of each curve gives the salinity-dependent freezing temperature.

boundary layer, ν the kinematic viscosity, and ΔT the temperature difference across the boundary layer.

Howard shows that the boundary layer is convectively unstable for

$$\mathrm{Ra}_\delta > 10^3, \tag{8b}$$

and argues that once the temperature layer becomes unstable, the layer consists of elements of water diffusively increasing in density until the local boundary layer becomes thick enough so that plumes of cold dense water separate from the layer and sink into the interior. In a related analysis relevant to the present work, Katsaros *et al.* (1977) extend Howard's work to the case of fluid cooled from above by a constant flux, and derive an instability criterion identical to (8). Even though both heat and salt are present in our problem, because the thermal layer is initially so much thicker than the salt layer, the criterion (8) should give a good approximation as to when the thermal layer becomes unstable. To apply (8b) to the layer of cold fluid below the salinity boundary layer, we first calculate β. To do this, we approximate the density dependence on s and T as

$$\rho = \rho(s)[1 - 7.5\times10^{-6}[T - 4 + 0.23s]^2], \tag{9a}$$

where

$$\rho(s) = 10^2 + 0.762s. \tag{9b}$$

The parabolic term in (9a) comes from a fit of the density dependence of fresh water to temperature near the temperature of maximum density (from Hodgman, 1955, p. 1972), and (9b) comes from a linear fit of density to salinity at 0°C (from Kaufman, 1960, p. 611). For the convective overturning, the temperature effect is the most important.

For $s = 38‰$ and $T = 0$°C, where these values are very nearly our far field conditions, Eqs. (9) give

$$\frac{1}{\rho}\frac{\partial \rho}{\partial s}\bigg|_T = 7.6\times10^{-4}, \tag{10a}$$

$$\beta = -\frac{1}{\rho}\frac{\partial \rho}{\partial T}\bigg|_s = 7.1\times10^{-5}\ ^\circ\mathrm{C}^{-1}. \tag{10b}$$

Comparison of (10a) and (10b) shows that the density perturbation caused by a salinity increase of $10^{-1}‰$ is of the same order as that caused by a temperature decrease of 1°C.

From Eqs. (9) and (10) and the solutions of the previous section, we next calculate the time in which the temperature-dominated part of the boundary layer becomes unstable. In the experiment our initial conditions were that $s = 37.6‰$ and $T_0 = -0.07$°C. From Figs. 6 and 7 and Eq. (1a), these conditions yield $T_w = -1.6$°C, $s_w = 27.8‰$, and $\lambda = 1.1\times10^{-2}$. From these values, we calculate $A = 1.51$°C and $B = 8.6$ in Eqs. (3a) and (3b). To estimate the salinity boundary layer thickness from (3b), we note that Eqs. (10) show that a density decrease caused by $\Delta s = 10^{-3}$ is cancelled by a temperature decrease of 10^{-2} °C. Use of the above value of B in (3b) shows that $\Delta s = s_0 - s = 10^{-3}$ when $u_s = 2.8$. Therefore, we choose $u_s = 2.8$ as the lower edge of the salinity boundary layer. Because $u_T = \epsilon u_s$, when $u_s = 2.8$, $u_T = 0.18$. From (3a) with the value of A given above, when $u_T = 0.18$, $T = -1.3$°C. Since $T_w = -1.6$°C and $T_0 = -0.07$°C, most of the temperature variation in the profile takes place below the salinity layer.

Therefore, to calculate Ra_δ, we choose δ in (8) as the distance from the wall, where we ignore the small part of the T layer which lies within the s layer, to that depth at which the temperature is within 99% of its far-field value. This gives

$$\delta = 3.8(\kappa t_c)^{\frac{1}{2}}, \tag{11}$$

where t_c is the time to the onset of convection.

Substitution of (11) into (8a), setting $\Delta T = 1.2$, and using $g = 9.8$ m s^{-2}, $\nu = 1.8\times10^{-6}$ m^2 s^{-1} (Kaufman, 1960, Table 68) and the previously given value of κ, we find that $t_c = 80$ s. For our choice of far-field conditions, where our salinity is slightly higher than that in the summer Arctic (Coachman and Aagaard, 1974), the diffusive boundary layer rapidly becomes unstable.

4. The combined conductive-turbulent regime

The discussion of Figs. 2–4 in Section 2 suggests that after the onset of instability the heat transfer takes place in three layers. First, between the ice bottom and the depth p shown on Figs. 2a–e, there is a conductive heat transfer layer; second, between the depths p and q, there is an unstable boundary layer; third, below q, there is a region of deep thermal convection.

a. The conductive boundary layer

Above the rms maximum or depth p, we model the heat transfer by the following assumptions. First, we assume that the salinity diffuses as if the temperature field did not exist. Second, because the temperature fluctuations at p are much smaller than ΔT_w, we approximate the temperature at p by the mean temperature T_s at that depth. Table 1, which lists the observed values of T_0, T_w and T_s for the same times correspond-

TABLE 1. Observed mean temperatures T_0, T_s and T_w and comparison of observed and predicted T_w at different times

Time (h)	T_0 (°C)	T_s (−°C)	T_w Observed (−°C)	T_w Predicted (−°C)
5.5	−0.09	0.3–0.4	1.04	1.04–1.09
7.5	−0.065	0.3–0.35	0.99	1.04–1.07
21.0	0.05	0.2	0.90	1.00
26.5	0.05	0.1	0.90	0.95
46.5	0.05	0.1	0.92	0.95

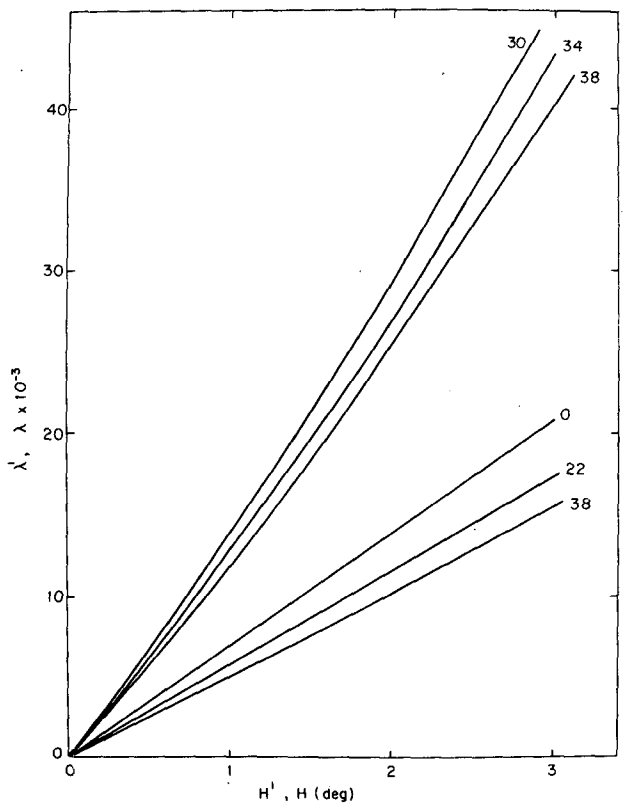

FIG. 8. The conductive boundary layer: the upper set of curves show λ' versus H' for the values of s_0 shown beside each curve. For comparison, the lower set of curves show λ versus H.

ing to Figs. 2a–e, shows that over the period of the experiment, the temperature T_s increases only very slowly with time. In this table, the uncertainty of the depth p causes the uncertainty of T_s. Third, we assume that the thickness of the conductive temperature layer increases with the same velocity as the diffusive salt layer, with the heat flux through the layer determined by the temperature difference across the layer.

Our coordinate system is nearly identical to Fig. 5. We again assume that $X(t)$ is the wall position and that the wall temperature is T_w. In addition we assume that at a depth $\delta_s(t)$, corresponding to the depth p shown in Fig. 2, the temperature is constant at T_s. We look for solutions to the one-dimensional diffusion equations of heat and salt which satisfy the boundary conditions

$$s=s_w, \quad T=T_w, \quad \text{at} \quad x=X(t), \tag{13a}$$

where we assume s_w and T_w constant. At the wall, the conditions (1) also hold.

The far-field conditions are that the temperature is constant at the edge of the salinity boundary layer, or

$$T=T_s, \quad \text{at} \quad x=\delta_s(t), \tag{13b}$$

while the salinity boundary condition is

$$s \to s_0 \quad \text{as} \quad x \to \infty. \tag{13c}$$

The solution for s therefore has the same form as (3b), so that

$$\delta_s(t)=2a(Dt)^{\frac{1}{2}}, \tag{13d}$$

where from the discussion in Section 3b, we set $a=2.8$. Finally, we assume that Eq. (4) again describes the wall position $X(t)$, with γ and λ now replaced by γ' and λ', where $\lambda'=\epsilon\gamma'$.

For a similar problem, MK (p. 517) show that the salinity layer thickness increases by only a negligible amount in the time necessary for the thermal profile to attain a steady state. Since the profile is steady and the temperatures at both $\delta_s(t)$ and $X(t)$ are assumed constant at T_s and T_w, respectively, the temperature must increase linearly with depth for $X(t) \leqslant x \leqslant \delta_s(t)$.

To solve for γ' and T_w in terms of T_s, we manipulate Eq. (3b) and the linear temperature profile in the same way as in Section 3a to obtain the solution

$$(a+\gamma')\gamma'=\alpha'[1-rf(\gamma')], \tag{14a}$$

where

$$\alpha'=\frac{H'k}{2L\rho_i D}. \tag{14b}$$

In (14), Eq. (7) defines $f(\gamma')$, and $H'=T_s+ms_0$ is the temperature elevation above the freezing point measured at the edge of the salinity boundary layer.

The difference in definition between α' and α in (6b) occurs because the themal boundary layer now diffuses at the same rate as the salt boundary layer. To show this, if in (6b) we replace κ by D and the scale factor $\pi^{\frac{1}{2}}$ by 2, we then obtain α'.

Given γ' from (14), we calculate T_w in terms of T_s as

$$T_w=T_s-\frac{H'}{\alpha'}[(a+\gamma')\gamma']. \tag{15}$$

We numerically solved (14) and (15) with an iterative technique for different values of T_s and s_0. Fig. 8 shows λ' as a function of s_0 and H'. Because the convective instability only occurs for $s>23‰$, we restrict the values of s in Fig. 8 to this range. On the same graph, we also plot the values of λ derived from the diffusive case. For $H=H'$, Fig. 8 shows that the wall melts about 2.5 times faster than the diffusive case. Fig. 9 shows T_w as a function of H_c and s_0; again comparison with Fig. 7 shows that as H' increases from zero, the wall temperature increases more rapidly in the present case.

From the observed values of T_s, we next compare the calculated values of T_w with the observed. The last two columns in Table 1 compare the observed and predicted values of T_w, where we calculate T_w from (15) and the observed range of T_s. The predicted values are close to the observed, although (except for the first case where the ice interior temperature is not uniform) generally slightly colder.

We also compare the theoretical and observed melt and growth rates of the ice front and the salinity boundary layer. Table 2 lists the observed and calculated values of $\delta_s(t)$ and $X(t)$. We measure $\delta_s(t)$ to an accuracy of ± 2 mm from the extrapolated depth of the rms maximum, and $X(t)$ visually from the scale attached to the thermocouple array. To calculate $X(t)$, we assume as an approximation from Table 1 that throughout the experiment T_s is constant at -0.1°C, so that from Fig. 8, $\lambda' = 2.7 \times 10^{-2}$. Substitution of this λ' into (4) gives the values of $X(t)$ listed in the second column, which are in fair agreement with the observed.

To calculate $\delta_s(t)$, we substitute $a = 2.8$ and $D = 6 \times 10^{-10}$ m^2 s^{-1} into (13d), where the resultant values are listed in the fourth column. The table shows that the calculated values are generally less than that observed, so that the boundary layer appears to spread faster than predicted.

There are two possible reasons for the difference between the theoretical and observed values of T_w and $\delta_s(t)$. Examination of Tables 1 and 2 shows that T_w is warmer than predicted and $\delta_s(t)$ is less than predicted. The largest change in $\delta_s(t)$ occurs between 21.0 and 26.5 h. Because $\delta_s(t)$ gives the depth of the rms maximum which occurs at a salinity equal to the far-field value minus a very small amount, any mixing, such as that generated by the drawing of water samples, may have been enough to move down the level p.

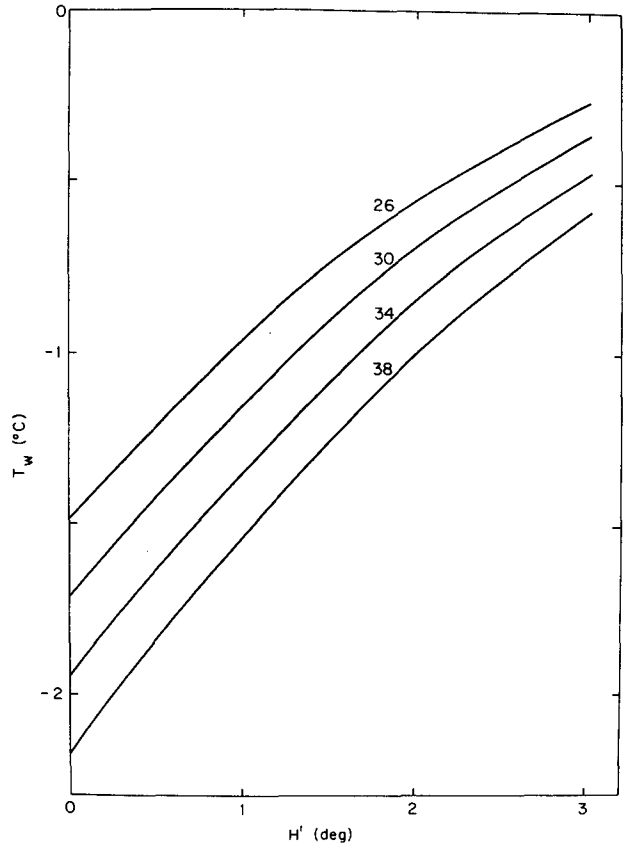

FIG. 9. The conductive boundary layer: T_w versus H' for the values of s_0 shown beside each curve.

TABLE 2. Comparison of observed and predicted values of $\delta_s(t)$ and $X(t)$.

Time (h)	$\delta_s(t)$ Observed (mm)	$\delta_s(t)$ Calculated (mm)	$X(t)$ Observed (mm)	$X(t)$ Calculated (mm)
5.5	22	19	2.0	2.8
7.5	32	23	3.0	3.3
21.0	39	38	6.3	5.5
26.5	62	42	7.2	6.2
46.5	72	56	9.5	8.2

A second source of error may be caused by the interaction of any sidewall heating with the interior stratification. Thorpe *et al.* [(1969), cited in Turner (1973), Section 8.2.3)] describe the convectively driven rolls which form when a salt-stratified fluid is heated or cooled from the side. In our case, because the salinity profile is close to an error function profile, at some depth below the ice the salinity gradient becomes weak enough so that very small differences between the wall temperature and the interior temperature would cause the formation of rolls. If these formed in our experiment, the additional mixing might increase the boundary layer thickness over that predicted.

Finally, to compare the melt rate calculated from the present conductive solution with that calculated from the diffusive case in Section 3a, we observe from Table 1 that away from the beginning of the experiment, the far-field temperature is nearly constant at $T_0 = +0.05$°C. For this temperature elevation, Fig. 6 gives $\lambda = 1.2 \times 10^{-2}$ for the diffusive case, whereas for the conductive case $T_0 = 0.05$°C corresponds to $T_s = -0.1$°C, which from Fig. 8 yields $\lambda' = 2.7 \times 10^{-2}$. Therefore in our experiment, the ice melts about 2.3 times faster for the conductive than for the diffusive heat transfer case.

b. The unstable boundary layer

Below the region of conductive heat transfer, from depth p to depth q in Fig. 2, we again have an unstable boundary layer. The top of this layer, or depth p, must be where the fluid is just marginally stable, since this fluid during its warmings and coolings experiences the largest temperature changes. Because at this depth we have a flux of both salt and heat from the underlying water toward the ice, the boundary layer differs from that described by Katsaros *et al.* (1977).

In our case, the heat flux destabilizes the underlaying water, whereas the salt flux stabilizes it. Therefore the boundary layer consists of water parcels being both rapidly cooled and slowly made less salty until the density is such that a parcel of cold, slightly less saline

TABLE 3. Observed values of δ', $Ra_{\delta'}$ and calculated values of δ' at different times.

Time (h)	δ' Observed (mm)	$Ra_{\delta'}$ ($\times 10^4$)	δ' Calculated (mm)
5.5	55	10	10–11
7.5	45	7	10
21.0	50	8	10
26.5	35	2	12
46.5	45	4	12

TABLE 4. Experimental values of Nu′, Ra′ and c at different times.

Time (h)	Nu′	Ra′ ($\times 10^6$)	c
5.5	130–60	193–286	0.19–0.10
7.5	59–45	217–263	0.10–0.073
21.0	44	231	0.075
26.5	54	138	0.109
46.5	47	138	0.094

water breaks away from the boundary layer. At this point, a parcel may undergo the double-diffusive instability called an "oscillatory instability" (see Turner, 1973, Section 8).

Because heat diffuses faster than salt, as the parcel falls, the surrounding waters warm the parcel without changing its salinity. This warming makes the parcel less dense than its surroundings so that the buoyant parcel rises back up to the depth p. Further, the heat gained by the parcel cools the surrounding water of salinity s_0 and thereby generates a region of pure thermal convection. Therefore, the unstable boundary layer should consist of two parts, a double-diffusive boundary layer above a purely thermal unstable boundary layer.

Our experimental evidence for this combined boundary layer is indirect; if we compare the observed boundary layer thickness with that calculated from the Rayleigh number criterion (8) for pure thermal convection, we find that the observed thickness is much greater than the calculated. Table 3 lists the observed boundary layer thickness δ' which we define as the distance from the depth p to q in Fig. 2. Using this δ' and $\Delta T_s = T_0 - T_s$ as the temperature difference across the boundary layer in (8a), we calculate the $Ra_{\delta'}$ listed in column 3 of the table; its values range from 30–100 times the critical value of 10^3. Finally, the last column lists the value of δ' which would occur if $Ra_{\delta'} = 10^3$. This δ' is about one-fifth of the observed value.

For the boundary layer to be caused by a simple thermal instability, either $\delta' \sim 10$ mm or $\Delta T_s \sim 10^{-2}$ °C. The absence of either of these conditions suggests that the mixed nature of the convection of the boundary layer causes the increased unstable boundary layer thickness.

c. *The deep thermal convection*

Below the unstable boundary layer, because the salinity is at its far-field value, the fluid motion should be purely thermally driven. To check this, we assume that the depth p, which is the only clearly defined level below the ice, is the upper surface of a convectively unstable fluid, then calculate for the experiment the Rayleigh number dependence of the Nusselt number Nu′ which we define as

$$\mathrm{Nu}' = \frac{Fd}{k\Delta T_s}. \tag{16}$$

In (16), F is the heat flux to the unstable fluid, d the tank depth below the level p which we assume constant at 0.70 m, $\Delta T_s = T_0 - T_s$, and the prime on Nu′ signifies that ΔT_s is measured only across one boundary layer. We calculate F from the conductive layer using

$$F = \frac{k\Delta T_w}{X(t) + \delta_s}, \tag{17}$$

where we take $\Delta T_w = T_s - T_w$ from Table 1, and $X(t)$ and δ_s from the observed values in Table 2.

The Rayleigh number Ra′ is given by

$$\mathrm{Ra}' = \frac{\beta g \Delta T_s d^3}{\nu\kappa}. \tag{18}$$

Substitution into (18) of $\Delta T_s \sim 10^{-1}$ °C from Table 1 and use of the other parameters listed in the text gives for our experiment that $\mathrm{Ra}' \sim 10^8$.

In this range, the only other experiments done to date on Rayleigh convection with both a free upper boundary and a flux boundary condition are those of Katsaros *et al.* (1977), who studied the convective instability of a water surface cooled by evaporation. From their experiments, they found that the dependence of Nu′ on Ra′ is

$$\mathrm{Nu}' = c\,\mathrm{Ra}'^{0.331}, \tag{19}$$

where $c = 0.156$ for their range of $3\times 10 < \mathrm{Ra}' < 4\times 10^9$.

Table 4 lists the values of Nu′, Ra′ calculated from (16) and (18) and the values of c calculated from (19) at the sample times of Figs. 2. From the table, c ranges from 0.075 to 0.19, with 0.1 as a good typical value. The table also shows that most of our values of c are significantly smaller than the value of 0.156 found by Katsaros *et al.* (1977). Because Eq. (19) shows that c decreases as ΔT_s increases, our reduced value of c may be caused by the mixed nature of our unstable boundary layer. Therefore, the mixed boundary layer reduces the heat transport below that predicted from pure Rayleigh convection.

5. Concluding remarks

In summary, comparison of the experiment and theory shows that an ice sheet floating on warm salty water with a salinity $>23‰$ melts through a combination of a conductive boundary layer and a deep thermal convection. In polar regions, this model is a possible mechanism for the enhancement of the melt rate at the bottom of thick pack ice and if the water below this ice is of a uniform salinity, provides for the generation of deep thermal mixing in the summer Arctic.

Acknowledgments. We thank James Murray for the use of his titration apparatus, and gratefully acknowledge the support of the Office of Naval Research under Task NR307-252 and Contract N00014-76-C-0234. Contribution 947 of the Department of Oceanography, University of Washington and Contribution 414 of the Department of Atmospheric Sciences, University of Washington.

REFERENCES

Caldwell, D. R., 1974: The effect of pressure on thermal and Fickian diffusion of sodium chloride. *Deep-Sea Res.*, **21**, 369–375.

Carslaw, H. S., and J. C. Jaeger, 1959: *Conduction of Heat in Solids.* Oxford University Press, 510 pp.

Coachman, L. K., and C. A. Barnes, 1962: Surface water in the Eurasian Basin of the Arctic Ocean. *Arctic*, **15**, 251–277.

——, and K. Aagaard, 1974: Physical oceanography of the Arctic Seas. *Marine Geology and Oceanography of the Arctic Seas*, Y. Rosenberg-Herman, Ed., Springer-Verlag, 1–72.

Frank, F. C., 1950: Radially symmetric phase growth controlled by diffusion. *Proc. Roy. Soc. London*, **A201**, 586–599.

Hodgman, C. D., Ed., 1955: *Handbook of Chemistry and Physics*, 37th ed. Chemical Rubber Publ. Co., 3156 pp.

Howard, L. H., 1966: Convection at high Rayleigh number. *Proc. 11th Intern. Congress Apl. Mech.*, H. Görtler, Ed., Springer-Verlag, 1109–1115.

Kaufman, D. W., Ed., 1960: *Sodium Chloride.* Reinhold, 749 pp.

Katsaros, K. B., W. T. Liu, J. A. Businger and J. E. Tillman, 1977: Heat transport and thermal structure in the interfacial boundary layer measured in an open tank of water in turbulent free convection. *J. Fluid Mech.* (in press).

Martin, S., and P. Kauffman, 1974: The evolution of under-ice melt ponds, or double diffusion at the freezing point. *J. Fluid Mech.*, **64**, 507–527.

Thorpe, S. A., A. Hall and I. Crofts, 1969: The effect of horizontal gradients on thermohaline convection. *J. Fluid Mech.*, **38**, 375–400.

Turner, J. S., 1973: *Bouyancy Effects in Fluids.* Cambridge University Press, 367 pp.